Journal of Inorganic Biochemistry 258 (2024) 112617

Contents lists available at ScienceDirect

Journal of Inorganic Biochemistry

journal homepage: www.elsevier.com/locate/jinorgbio

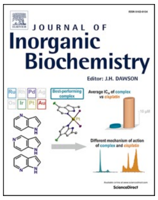

Pt(II) *Bis*(pyrrole-imine) complexes: Luminescent probes and cytotoxicity in MCF-7 cells†

Sheldon Sookai [a,*], Shanen Perumal [b], Mandeep Kaur [b], Orde Q. Munro [a,c]

[a] *Molecular Sciences Institute, School of Chemistry, University of the Witwatersrand, PO WITS 2050, Johannesburg, South Africa*
[b] *Research Unit, School of Molecular and Cell Biology, University of the Witwatersrand, Johannesburg 2050, South Africa*
[c] *School of Chemistry, University of Leeds, Woodhouse Lane, Leeds LS2 9JT, UK*

ARTICLE INFO

Keywords:
Cytotoxicity
Albumin
Theranostic
Phosphorescence
Schiff base
MCF-7

ABSTRACT

Four Pt(II) *bis*(pyrrole-imine) Schiff base chelates (**1**–**4**) were synthesised by previously reported methods, through a condensation reaction, and the novel crystal structure of 2,2′-{propane-1,3-diyl*bis*[nitrilo(*E*)methyl-ylidene]}*bis*(pyrrol-1-ido)platinum(II) (**1**) was obtained. Pt(II) complexes **1**–**4** exhibited phosphorescence, with increased luminescence in anaerobic solvents or when bound to human serum albumin (HSA). One of the complexes shows a 15.6-fold increase in quantum yield when bound to HSA and could be used to detect HSA concentrations as low as 5 nM. Pt(II) complexes **1**–**3** was investigated as potential theranostic agents in MCF-7 breast cancer cells, but only complex **3** exhibited cytotoxicity when irradiated with UV light ($\lambda_{355\ nm}^{Excitation}$). Interestingly, the cytotoxicity of complex **1** was unresponsive to UV light irradiation. This indicates that only complex **3** can be considered a potential photosensitising agent.

1. Introduction

Schiff bases comprising of an imine group have for decades drawn the interest of researchers due to their relative ease of synthesis, unique roles in pharmaceuticals [1,2] and their ability to form complexes with transition metal ions. Complexes of Schiff base imines are an attractive class of complexes due to their versatility in fields such as photophysics [3–5], catalysis [6], investigating anticancer drug candidates [7,8], and their uses in biological applications [7,9]. Focusing on biological activity of Schiff base complexes several transition metal complexes have been reported to possess anti-bacterial, anti-microbial, antiviral, anti-malarial and anti-inflammatory properties [10–13]. The impressive biological activity of Schiff base ligands compounds is due to their synthetic flexibility and structural stability.

The well-known Pt(II) complexes cisplatin, carboplatin and oxaliplatin are widely administrated and successful anticancer drugs [14]. Unfortunately, they cause severe side effects [15] and certain cancer types may become drug resistant [16,17]. This has prompted the search for novel Pt-based anticancer agents with diminished toxicity and unique modes of action. These include Pt(IV) prodrugs that upon administration are reduced within a cell matrix or are reduced by irradiated light to the more active Pt(II) species [18–20]. Efforts have been made to develop theranostic and/or photodynamic therapeutic (PDTs) agents [7,8,21,22]. Metal-based theranostic compounds consists of either Ir(III) [23–26], Ru(II) [27–29], Re(I) [30–32], or Pt(II) [7,8,21,22], while less common heavy metal centres are Rh(III), Os(II) [33–35] and Pd(II) [36]. The heavy metal centre coupled with the organic ligand framework results in the compound's ability to phosphoresce via metal-to-ligand charge transfer (MLCT) transitions. Theranostic agents serve as diagnostic and therapeutic tools [37]. Key characteristics of phosphorescent heavy metal complexes employed as diagnostic tools typically in bioimaging are (i) large Stokes shifts, (ii) high quantum yields, (iii) photosensitivity, (iv) two photon absorption cross section and, (v) based on the organic ligand framework, targeting of specific cellular organelles [38,39]. From a therapeutic aspect selected heavy metal complexes target cancer cells by one of two mechanisms: (i) generation of reactive oxygen species (ROS) such as $O_2^{\bullet-}$ and OH• [40] or (ii) more commonly by direct energy transfer from the photosensitiser to $^3O_2$, converting it to $^1O_2$ [27]. Heavy metal ions that do this may also be referred to as PDTs. Currently there are two PDT agents undergoing clinical trials WST11 (a Pd(II) bacteriopheophorbide derivative) [36,41] and TLD-1433 (a polypyridyl Ru(II) complex) [27,42]. During the development of effective therapeutic agents, it is important to understand their interaction with human serum albumin

---

* Corresponding author.
E-mail address: Sheldon.sookai@wits.ac.za (S. Sookai).

https://doi.org/10.1016/j.jinorgbio.2024.112617
Received 28 March 2024; Received in revised form 20 May 2024; Accepted 22 May 2024

(HSA). HSA is the most abundant plasma protein, occurring at concentrations of 600 μM [43]. The two main functions of HSA are to maintain osmotic pressure and to transport both endogenous and exogenous compounds [44]. Furthermore, delineating the interaction of drug-like molecules with HSA is key to understanding their pharmacokinetic and pharmacodynamic data. When some phosphorescent heavy metal complexes bind to HSA there is a "switch on, light effect" characterised by an increase in the quantum yield of the heavy metal complex. This is useful in bioimaging and may serve as a method to understand the mechanism by which HSA transports heavy metal complexes to tumors [37]. There have been few studies on the application of Pt(II) Schiff base complexes as a theranostic or PDT agents [7].

Here we report the synthesis of four Pt(II) chelates (**1**–**4**) and the crystal structure of one of them, square planar 2,2′-{propane-1,3-diyl*bis*[nitrilo(E) methylylidene]}*bis*(pyrrol-1-ido)platinum(II) (**1**). The electronic absorption and emission spectra were studied under different conditions and reported as a relative quantum yield. Lastly, we examined the cytotoxicity of Pt(II) complexes **1**–**3** in MCF-7 human breast cancer cells and NMuMG non-transformed mouse mammary cells in the presence and absence of irradiation with UV-light.

2. Experimental section

All solvents (HPLC grade) and chemical synthons (pyrrole-2 carboxaldehyde and diamines) were used as received from Merck Sigma-Aldrich® without further purification. Deuterated dimethyl sulfoxide was stored over activated 4 Å molecular sieves. Human serum albumin (HSA) 99% purity was purchased from Sigma and used as received without further purification. Ultrapure water (Type I) was produced using a Merk-Millipore Direct-Q® 3 UV Water Purification System.

3. Instrumentation and basic methods

Crystallography. Single crystal X-ray structure determinations were carried out with a four-circle Bruker D8 Venture X-ray diffractometer equipped with a Photon II CPAD area detector and a fine-focus sealed X-ray tube source (Mo anode). Crystals were mounted under Paratone® oil on nylon loops (Hampton Research) and the crystals were kept at 173(1) K during data collection (Oxford CryoStream 700). Using Olex2 [45], the structures were solved with the ShelXT2 [46] structure solution program (intrinsic phasing) and refined with ShelXL3 [47] using least squares minimisation.

General spectroscopy. Proton and carbon NMR spectra were recorded on Bruker Avance III 400 and 300 NMR spectrometers at ^{1}H frequencies of 400 and 300 MHz, respectively, and ^{13}C frequencies of 100 and 75 MHz, respectively. Spectra were recorded at 298 K with 5 mm BBOZ or TBIZ probes. Chemical shifts for both proton and carbon were reference using the solvent signal. MestReNova (version 14.2.1–27,684) was used to analyse NMR spectra. FTIR spectra of powder samples were recorded using a Bruker Alpha FTIR spectrometer incorporating a Bruker Platinum® diamond ATR sampling accessory. Spectra were analysed using the OPUS software package on the spectrometer (version 7.5). Mass spectra were recorded with Bruker Compact Q-TOF high-resolution mass spectrometer using Bruker Daltronics HyStar 3.2 SR4 software. Bruker Compass DataAnalysis software (Version 4.3) was used to analyse chromatograms. Samples of pure compounds (typically ca. 10 μg/mL) were prepared in HPLC grade acetonitrile or ethanol for metal chelates and HPLC grade methanol for ligands. Solutions were acidified using 0.1% (V/V) formic acid to obtain spectra in ESI+ mode. Electronic spectra were recorded using either a PerkinElmer Lambda 365 double beam spectrometer connected to a Peltier controller and multicell thermostatic cell block or an Analytik Jena Specord210 Plus double-beam instrument fitted with an external water circulating thermostatic bath and thermostatted cell holders. The spectral data were analysed with the spectrometer software or Origin Pro 2023b. Spectra were recorded (10-mm pathlength quartz cuvettes) as a function of concentration for both characterisation and the determination of molar absorptivity constants.

Compound synthesis. All *bis*(pyrrole-imine) chelates and Pt(II) *bis* (pyrrole-imine) chelates were synthesised by methods previously reported [4,48,49].

Ligand characterisation. *N,N′-bis*[(1*E*)-1H-pyrrol-2-ylmethylene] propane-1,3-diamine (H_2PrPyrr). ^{1}H NMR (400 MHz, chloroform-d, 300 K) [δ, ppm]: 8.03 (s, 2H, H-5), 6.88 (t, $J = 1.9$ Hz, 2H; H-1), 6.48 (dd, $J = 3.6$, 1.4 Hz, 2H; H-3), 6.23 (dd, $J = 3.6$, 2.6 Hz, 2H; H-2), 3.61 (td, $J = 6.8$, 1.2 Hz, 4H; H-6), 1.98 (t, $J = 6.8$ Hz, 2H; H-7). ^{13}C NMR (101 MHz, chloroform-d, 300 K) [δ, ppm]: 151.85 (C-5), 129.86 (C-4), 122.04 (C-1), 114.13 (C-3), 109.59 (C-2), 57.80 (C-6), 32.29 (C-7). IR (KBr pellet, cm^{-1}): 3112w δ(NH, pyrrole), 3053 m br ν(CH, imine), 2941 m ν(CH, $CH_2CH_2CH_2$), 2847 ν(CH, CH_2-N=CH), 1634s br ν(C=N). UV–vis (ethanol) [λ_{max}/nm, ε/mol^{-1} dm^{3} cm^{-1}]: 289, 3.20 × 10 [4].

1,3-*bis*{ [(1*E*)-1*H*-pyrrol-2-ylmethylene] amino}propan-2-ol (H_2(OH)Pyrr). ^{1}H NMR (400 MHz, DMSO-d_6–300 K) [δ, ppm]: 11.34 (s br, 2H, DMSO-d_6 exchangeable, H-9), 8.07 (s, 2H; H-5), 6.87 (t, $J = 1.9$ Hz, 2H; H-1), 6.44 (dd, $J = 3.5$, 1.5 Hz, 2H; H-3), 6.11 (t, $J = 3.0$ Hz, 2H; H-2), 4.00–3.82 (m, 1H; H-7), 3.77–3.54 (m, 2H; CH_2-N=CH), 3.43 (dd, $J = 11.7$, 6.5 Hz, 2H; CH_2-N=CH). ^{13}C NMR (101 MHz, DMSO-d_6, 300 K) [δ, ppm]: 152.92 (C-5), 130.41 (C-4), 122.03 (C-1), 113.35 (C-3), 108.98 (C-2), 70.69 (C-7), 65.14 (C-6). IR (KBr pellet, cm^{-1}): 3254w (NH, pyrrole), 3088 m (CH, imine), 2882 (CH, H-COH), 2859 (CH, CH_2-N=CH), 1633s (C=N), 1127 (C—O stretch). UV–vis (ethanol) [λ_{max}/nm, ε/mol^{-1} dm^{3} cm^{-1}]: 289; 3.23 × 10^{4}.

2,2-dimethyl-*N,N′-bis*[(1*E*)-1*H*-pyrrol-2-ylmethylene] propane-1,3-diamine ($H_2(CH_3)_2$Pyrr). ^{1}H NMR (400 MHz, chloroform-d, 300 K) [δ, ppm]: 9.50 (s br, 2H; H-9), 7.99 (t, $J = 4.2$ Hz, 2H; H-5), 6.90 (d, $J = 6.1$ Hz, 2H; H-1), 6.48 (dt, $J = 6.6$, 3.4 Hz, 2H; H-3), 6.26 (p, $J = 3.2$ Hz, 2H; H-2), 3.46 (t, $J = 4.2$ Hz, 4H; H-6), 0.97 (t, $J = 4.3$ Hz, 6H; H-8). ^{13}C NMR (101 MHz, chloroform-d 300 K) [δ, ppm]: 152.17 (C-5), 130.06 (C-4), 122.20 (C-1), 114.28 (C-3), 109.44 (C-2), 69.32 (C-6), 36.96 (C-7), 24.28 (C-8). IR (KBr pellet, cm^{-1}): 3130 m br ν(CH, imine), 2966 m ν (CH, terminal CH_3), 2852 m ν(CH_2, alkyl), 1635s br ν(C=N). UV–vis (ethanol) [λ_{max}/nm, ε/mol^{-1} dm^{3} cm^{-1}]: 289; 3.23 × 10^{4}.

(1*R*,2*R*)-*N,N′-bis*[(1*E*)-1*H*-pyrrol-2-ylmethylene] cyclohexane − 1,2-diamine (H_2(−R cyclohexane)Pyrr. ^{1}H NMR (400 MHz, DMSO-d_6, 300 K) [δ, ppm]: 11.16 (s, 2H; H-9), 7.94 (s, 2H; H-5), 6.76 (t, $J = 1.9$ Hz, 2H; H-1), 6.31(dd, $^{3}J_1 = 3.5$ Hz, $^{3}J_2$ 1.4 Hz, 2H; H-3), 6.01 (t, $J = 3.0$ Hz, 2H; H-2), 3.23 (m, 2H; H-6), 1.34–1.80 (m, 8H, H-7 and H-8). ^{13}C NMR (101 MHz, DMSO-d_6, 298 K) [δ, ppm]: 24.70 (C-8), 33.85 (C-7), 74.09 (C-6), 109.07 (C-2), 113.61 (C-3), 122.08 (C-1), 130.33 (C-4), 151.26 (C-5). UV–vis (acetonitrile) [λ_{max}/nm, ε/mol^{-1} dm^{3} cm^{-1}]: 289; 2.95 × 10^{4}.

Pt(II)-chelate characterisation. 2,2′-{propane-1,3-diyl*bis* [nitrilo(*E*)methylylidene] }*bis*(pyrrol-1-ido)platinium(II) (1). ^{1}H NMR (400 MHz, DMSO-d_6, 300 K) δ 8.15 (s, 2H; H-5), 7.19 (s, 2H; H-1), 6.64 (d, $J = 3.7$ Hz, 2H; H-3), 6.16 (dd, $J = 3.7$, 1.8 Hz, 2H; H-2), 3.73 (m, 4H; H-7), 1.94 (p, $J = 4.5$ Hz, 2H; H-6). ^{13}C NMR (101 MHz, DMSO-d_6, 300 K) δ 160.72 (C-5), 140.83 (C-4), 135.41 (C-1), 117.31 (C-3), 110.92 (C-2), 54.29 (C-6), 32.02 (C-7). UV–vis (acetonitrile) [λ_{max}/nm, ε/mol^{-1} dm^{3} cm^{-1}]: 279, 1.67 × 10^{4}; 304, 1.40 × 10^{4}; 334, 1.31 × 10^{4}; 385, 8.56 × 10^{3}. IR (KBr pellet, cm^{-1}): 3083 m br ν(CH, imine), 2914 m ν(CH, CH_2-N=CH), 1582s br ν(C=N). HRMS (m/z): [M + H] + calcd. For $C_{13}H_{14}N_4Pt$, 422.0942.

422.0970.**2,2′-{(2-hydroxypropane-1,3-diyl)*bis*[nitrilo(*E*) methylylidene] } *bis*(pyrrol-1-ido) platinum(II) (2**). ^{1}H NMR (400 MHz, DMSO-d_6) δ 8.19 (s, 1H; H-5), 7.20 (s, 2H; H-1), 6.65 (d, $J = 3.8$ Hz, 2H; H-3), 6.17 (dd, $J = 3.8$, 1.9 Hz, 2H; H-2), 5.30 (d, $J = 4.5$ Hz, 1H; H-8)), 4.03–3.95 (m, 2H; H-7), 3.82 (d, $J = 14.0$ Hz, 2H; H-6), 3.66 (dd, $J = 14.1$, 7.6 Hz, 2H; H-6). ^{13}C NMR (101 MHz, DMSO-d_6) δ 161.75 (C-5), 140.88 (C-4), 135.52 (C-1), 117.25 (C-3), 110.84 (C-2), 70.47 (C-7), 59.76 (C-6). IR (KBr pellet, cm^{-1}): 3083 (CH, imine), 2990 (CH, H-COH), 2904 (CH, CH_2-N=CH), 1575 (C=N), 1126 (C—O stretch). UV–vis (acetonitrile) [λ_{max}/nm, ε/mol^{-1} dm^{3} cm^{-1}]: 277, 1.64 × 10^{4};

303, 1.91 × 10^4; 313, 2.11 × 10^4; 382, 1.55 × 10^4.

2,2′-{(2,2-dimethylpropane-1,3-diyl)*bis*[nitrilo(*E*)methylylidene]} *bis*(pyrrol-1-ido) platinum(II) (3). ^{1}H NMR (400 MHz, DMSO-d_6) δ 8.16 (s, 2H; H-5), 7.21 (s, 2H; H-1), 6.66 (d, $J = 3.8$ Hz, 2H; H-3), 6.18 (dd, $J = 3.9$, 1.9 Hz, 2H; H-2), 3.48 (s, 4H; H-6), 1.05 (s, 6H; H-8). ^{13}C NMR (101 MHz, DMSO-d_6) δ 161.23 (C-5), 140.78 (C-4), 135.44 (C-1), 117.21 (C-3), 110.88 (C-2), 64.52 (C-6), 38.78 (C-7), 23.90 (C-8). IR (KBr pellet, cm^{-1}): 3085 (CH, imine), 3015 m(CH, terminal CH$_3$), 2933 (CH2, alkyl), 1652 (C=N). IR (cm^{-1}): 2919 m br ν(CH, imine), 1566s br ν(C=N). UV–vis (acetonitrile) [λ_{max}/nm, ε/mol^{-1} dm^3 cm^{-1}]: 277, 1.64 × 10^4; 303, 1.85 × 10^4; 313, 2.06 × 10^4; 382, 1.51 × 10^4.

2,2′-{(1*R*,2*R*)-cyclohexane-1,2-diyl*bis*[nitrilo(*E*)methylylidene]}*bis*(pyrrol-1-ido)platinum(II) (4). ^{1}H NMR (400 MHz, DMSO-d_6) δ 8.15 (s, 2H; H-5), 7.10 (s, 3H; H-1), 6.64 (d, $J = 3.8$ Hz, 3H; H-3), 6.14 (dd, $J = 3.9$, 1.8 Hz, 3H; H-2), 4.03–3.80 (m, 3H; H-7), 2.56 (s, 1H; H-6), 1.75 (d, $J = 8.7$ Hz, 3H; H-8), 1.57–1.42 (m, 3H; H-8), 1.34 (t, $J = 10.3$ Hz, 7). ^{13}C NMR (101 MHz, DMSO-d_6) δ 153.82 (C-5), 145.15 (C-1), 136.74 (C-4), 118.43 (C-3), 110.20 (C-2), 73.88 (C-6), 27.82 (C-7), 24.06 (C-8). IR (KBr pellet, cm^{-1}): 2919 m br ν(CH, imine), 1566s br ν(C=N). UV–vis (acetonitrile) [λ_{max}/nm, ε/mol^{-1} dm^3 cm^{-1}]: 277, 1.89 × 10^4; 303, 1.73 × 10^4; 316, 1.89 × 10^4; 382, 2.04 × 10^4.

Fluorescence emission spectroscopy. Appropriate amounts of each of the four Pt(II) *bis*(pyrrole-imine) chelates were weighed and dissolved into either acetonitrile or DMSO to obtain a 5 × 10^{-3} M stock solution. After dilution of the Pt(II) chelates, in KH$_2$PO$_4$ buffer, samples were centrifuged at 10000 xg for 10 min (Hettich® Mikro220R microcentrifuge) to ensure no precipitate had formed. The fluorescence emission spectrum was achieved by diluting the stock solutions of **1**–**4** to 10 × 10^{-6} M in either acetonitrile or KH$_2$PO$_4$ (50 mM, pH 7.5) and were measured on a Cary Eclipse fluorescence spectrophotometer (Varian, Australia) equipped with a 1.0 cm quartz cell and a circulating thermostat bath. Excitation and emission slit widths were fixed at 10 nm. The Pt(II) *bis*(pyrrole-imine) chelates were excited at 382 nm and the fluorescence emission was measured from 500 nm to 750 nm.

Fluorescence emission spectroscopy of deoxygenated Pt(II) *bis*(pyrrole-imine) chelates. Pt(II) *bis*(pyrrole-imine) chelates (10 × 10^{-6} M) in either acetonitrile or KH$_2$PO$_4$ (50 mM, pH 7.5; the pH was 7.5 after adjusting the solution with KOH) were bubbled with argon gas for 3 min before the fluorescence emission spectrum was measured as described above.

Quantum yields calculated by a relative method.

$$\Phi F = (As)\Big/Ax\Big)(Fx/Fs)(nx/ns)^2 \tag{1}$$

The relative quantum yields (ΦF) of the Pt(II) chelates were determined by previously reported methods [50,51]. **4** was used as the standard reference as its quantum yield had been previously determined [4]. Using eq. 1 the relative quantum yields for **1**, **2** and **3** were determined in acetonitrile, dichloromethane (DCM), and dH$_2$O (deionised water), when bound to HSA and in the absence of O$_2$. The Pt(II) chelates were dissolved in the respective solvents and were diluted until their absorbance was between 0.01 and 0.1. The same sample's $\lambda^{Emission}$ was then measured between 500 and 750 nm. Each of the samples were measured in triplicate. The area under the fluorescence emission spectrum for the Pt(II)-chelates and the respective solvents was measured using Origin Pro 2023b. Area of the solvent was subtracted from the area of the Pt(II)-chelate in the solvent as a blank. Finally, we plotted the curve area of each Pt(II)-chelate emission spectrum against its absorption spectrum to calculate the relative quantum yield using eq. 1. For eq. 1 ΦF is the relative quantum yield, *As* and *Ax* are the absorbances of the unknown sample and the reference. *Fx* and *Fs* are the areas under the fluorescence emission spectrum curves for the unknown samples and the reference sample respectively. Finally, n represent the refractive indicies of the respective solvents. The refractive indexes for dH$_2$O, acetonitrile and DCM were taken as 1.333, 1.3441 and 1.4241 respectively [52].

TD-DFT simulations. Simulations were performed to calculate optimised structures, vibrational frequencies, and electronic spectra for **1**, **2** and **3** using Gaussian 16 Rev. C.01 [53] at the CAM-B3LYP [54]/DEF2-QZVP [55] level of theory using the GD3BJ empirical dispersion correction [56]. Structures were also calculated using the SDD basis set [57]. The default geometry convergence criteria in Gaussian 16 were applied. Nuclear shielding tensors were calculated by the default GIAO method [58,59] in Gaussian. Simulations were carried out in vacuo and in acetonitrile solvent continua (SCRF PCM method [60]). GaussView 6.0.16 [61] was used for preparing input files and data visualisation. GaussSum 3.0 was used to visualise electronic spectra and tabulate transition assignments [62]. All geometry-optimised structures were characterised by positive frequency eigenvalues, indicating that true minima were located on the global potential energy surface for each system. Time-dependent DFT (TD-DFT) simulations were carried out using the above method (CAM-B3LYP) and basis sets in Gaussian 16 for all small molecules. Typically, 60 excited singlet states were computed to cover the full spectral range (150–900 nm).

Fluorescent microscopy. Intracellular localisation and fluorescence were determined using fluorescent microscopy. NMuMG cells were seeded at a density of 20,000 cells per well onto 12 mm glass coverslips in a 24-well plate. After incubation at 37 °C for 24 h, cells were treated with 10 μM Pt(II) complexes with the addition of 10 μM HSA, or a dH$_2$O control for 2 h at 37 °C, followed by fixation with 4% formaldehyde for 10 min. Nuclei were stained with NucRed™ Dead (Thermo Fisher Scientific, USA). Cells were visualised using the Floid™ Cell Imaging System (Thermo Fisher Scientific, USA).

Cytotoxicity assays. Cytotoxicity assays were performed to assess the changes in cell viability following treatment of NMuMG (non-transformed mouse mammary gland epithelial cells) and MCF7 (human epithelial breast cancer cells) with the Pt(II) complexes. The MTT assay is a colorimetric assay used to assess cell viability based on the reduction of the yellow 3-(4,5-dimethylthiazol-z-yl)-2,5 diphenyltetrazolium bromide (MTT) to its purple insoluble formazan crystals in the mitochondria of viable cells. Cells were seeded in a 96-well plate at a density of 5000 cells per well. After incubation at 37 °C for 24 h, cells were treated with chelates 1–3 diluted in DMSO to varying concentrations (0–250 μM) for 24 h at 37 °C. Formazan crystals were dissolved in solubilising solution overnight at 37 °C and optical density was measured at a wavelength of 570 nm using a Multiskan GO Microplate Reader (Thermo Fisher Scientific. USA). Percentage cell viability was calculated relative to the untreated control. Plumbagin (PL) was dissolved in DMSO (Sigma-Aldrich, Dorset, UK) and further diluted in media to achieve the treatment dose of 40 μM. PL was utilised as a positive control based on previous studies indicating its cytotoxic effects [63].

UV-light exposure cytotoxicity experiments: The MCF-7 and NMuMG cells were treated with the three Pt(II) chelates **1**–**3** (0–250 μM) exposed to indigo light irradiation (10 min, 355 nm), then the cells were further incubated for 24 h. The cells were carefully transferred into flat-bottomed 96-well plates and pipette-mixed for the MTT assay. IC$_{50}$ values were determined in triplicates and their standard deviations were calculated as above.

4. Molecular docking

Molecular docking experiments were conducted by previously reported methods by Sookai et al. [64]

5. Results and discussion

5.1. Synthesis and X-ray crystallography

Four Pt(II) *bis*(pyrrole-imine) chelates (**1**–**4**) were synthesised and characterised by previously reported methods [4,48,49] and are depicted in Scheme 1. Purification by recrystallisation followed by X-ray crystallography afforded a novel crystal structure for **1**. Complexes **2**–**4**

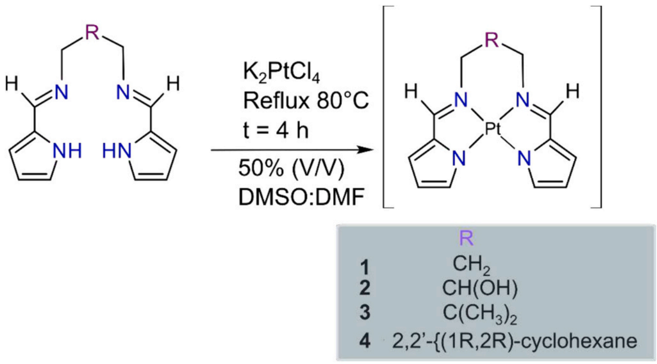

	R
1	CH$_2$
2	CH(OH)
3	C(CH$_3$)$_2$
4	2,2'-{(1R,2R)-cyclohexane

Scheme 1. Schematic synthesis procedure for the metalation of the four *bis* (pyrrole-imine) ligands with K$_2$PtCl$_4$ relevant to this work.

had been previously reported and were not studied by X-ray diffraction methods [4,49]. Reaction scheme 1, provides a brief outline on the synthetic route used. In brief the appropriate *bis*(pyrrole-imine) chelate was metalated with Pt(II) by reaction with K$_2$PtCl$_4$. Complex **4** was obtained without any impurities from the method described previously,[4] while **2** and **3** were prepared by a similar method to **4**. The novel crystal structure for complex **1** was obtained by slow liquid diffusion of a DCM solution of the metal chelate into hexane (non-solvent). (See Schemes 2 and 3.)

The ^{1}H NMR (Figs. S1, 4, 7 and 10) for Pt(II) chelates **1**–**4** highlight the salient spectroscopic features of this class of compounds. Complexes **2**–**4** have been previously discussed [49], therefore we analysed the ^{1}H NMR of complex **1**. The imine proton (N=C–H) resonates as a singlet at 8.15 ppm (DMSO-d_6), downfield from that of the Ni(II) congener (δ_H = 7.58 ppm, DMSO-d_6) [48], complex **2** (8.20) [49] and both enantiomers of **4** in CDCl$_3$ (δ_H = 7.61 ppm) [4]. Complexes **3** and **4** give similar imine CH signals to **1** (δ_H = 8.15 and 8.16 ppm, respectively), highlighting that the differences in solvent polarity leads to significant proton chemical shift variations for Pt(II) *bis*(pyrrole-imine) chelates. Significantly, spin–spin coupling ($^3J\{^1H,^{195}Pt\}$) of the imine CH proton to ^{195}Pt (33.8%) [65] culminates in discernible satellite peaks flanking the 8.15-ppm resonance. The coupling constant $^3J_{Pt\text{–}H}$, for **1** (72.20 Hz) is similar to complexes **2**, and **3**, previously reported [49]. $^3J_{Pt\text{–}H}$, are similar, measuring 72.14, and, 72.63, respectively. This is beyond the range reported for complexes with three-centre N–H···Pt(II) interactions ($^1J_{Pt\text{–}H}$ = 33–55 Hz) [66] and simple *cis* and *trans* square planar PtI$_2$(NH$_2$R)$_2$ complexes ($^3J_{Pt\text{–}H}$ = 35–49 Hz) [67]. The pronounced spin-spin coupling observed is a clear indication of the rigid, flat configuration of the *bis*(pyrrole-imine) chelate. This chelate imposes Pt-N-C-H torsion angles, ϕ, of ~180°, ensuring optimal ^{1}H—^{195}Pt coupling (based on the Karplus equation) [68]. The strong $^3J_{Pt\text{–}H}$ spin couplings for **1** are as expected comparable to the $^3J_{Pt\text{–}H}$ spin couplings for **2**–**4**, the $^2J\{^1H,^{195}Pt\}$ coupling (~60 Hz) reported for *trans*-[Pt(ethene)(2-carboxypyridine)Cl] [69] and the 58–70 Hz $^2J\{^1H,^{195}Pt\}$ couplings for all geometric isomers of the former PtI$_2$(NH$_2$R)$_2$ complexes [67].

The single crystal of **1** obtained by slow liquid diffusion was a dark red rhombic crystal. Complex **1** (Fig. 1a) crystallised in a monoclinic P2$_1$/c space group, the Pt(II) metal ion centre adopts a four-coordinate square planar geometry. The asymmetric unit (ASU) of **1** comprises four independent molecules (A–D; Fig. 1b), each having the square planar Pt(II) ion chelated by the tetradentate *bis*(pyrrole-imine) ligand. The Pt–N$_{pyrrole}$ and Pt–N$_{imine}$ distances average 2.013(4) and 2.003(4) Å, respectively (Table S1). These bond distances are statistically equivalent to the mean Pt–N$_{pyrrole}$ and Pt–N$_{imine}$ values of the chiral Pt(II) (*R*,*R*)-(−)- and (*S*,*S*)-(+)-1,2-*bis*(pyrrol-2-ylmethyleneamino)cyclohexane ligands reported by Shan et al.[4]

Typically, the sum of the angles around a square planar metal centre equate to 360°. The sum of the angles around **1** was 351°(16). The slightly nonplanar conformations of the ligands mainly reflect non-bonded crystal packing interactions and the formation of discrete, stacked dimers. In Fig. 1b, the dimer formed by molecules A and B is face-to-face (in an inverted relative orientation) with a Pt1A···Pt1B separation of 3.732(1) Å, PtN4 plane centroid-to-centroid (Ct···Ct) distance of 5.061(4) Å, mean plane separation (MPS$_{AB}$) of 4.020(1) Å, (Fig. 1). Both *bis*(pyrrole-imine) chelates curve inwards towards the intradimer space. The dimer formed by molecules C and D is similar to that formed by molecules A and B, with a face-to-face, relative inverted orientation of the two monomers. Molecules C and D exhibit a Pt1C···Pt1D separation of 3.800(1) Å, a Ct···Ct distance of 5.189(4) Å, and MPS$_{CD}$ of 3.606(4) Å and curve inwards towards the intradimer space. The Pt···Pt bond distances are >3.5 Å which is double the van der Waals radius of the Pt atom [70] and fall outside the range of dz$_2$(Pt)–dz$_2$(Pt) orbital interactions. These distances are consistent with weak (metal-metal) d^8 interactions.

5.2. UV–visible spectra and DFT simulations of the Pt(II) chelates

The experimental UV–vis spectrum of **1** is presented in Fig. 2a and was assigned by analysis of the TD–DFT-calculated spectrum of the complex. The spectra for complexes **2**–**4** have been previously reported [4,49] but for comparison have been calculated and presented in Figs. S13, 17 and 18. The DFT calculated electronic spectrum of **1**, excluding the vibronic transitions, showed a reasonably good correlation with the experimental spectrum after implementing a 56 nm red-shift correction to the band energies and appropriate scaling of the intensities (ε- values). In the visible region for complex **1**, the band at 454 nm (1st excited state) is assigned to the HOMO → LUMO transition; the maximum at 427 nm is the corresponding transition to the first excited vibrational level of the excited state. Analysis of the molecular orbitals

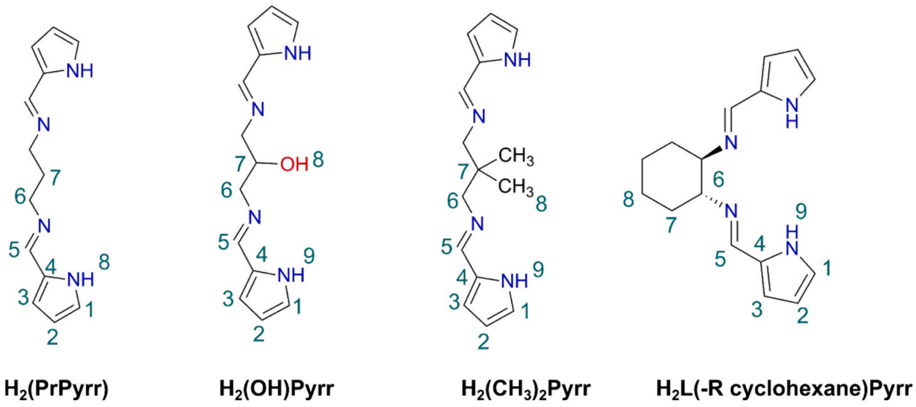

Scheme 2. Structures of the ligands synthesised in this study showing the atom numbering sequence.

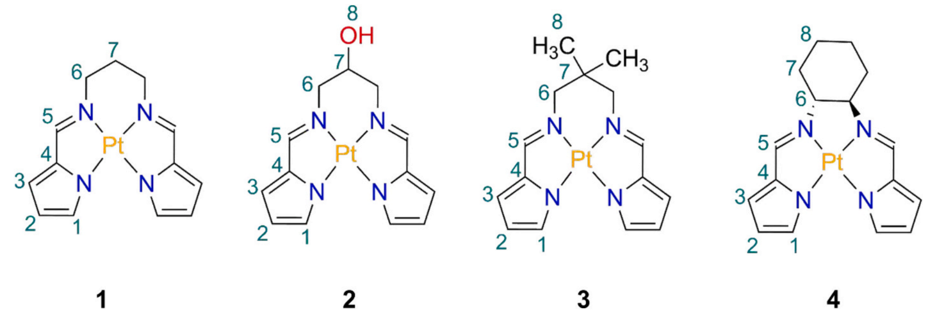

Scheme 3. Structures of the Pt(II) chelates synthesised in this study showing the atom numbering sequence.

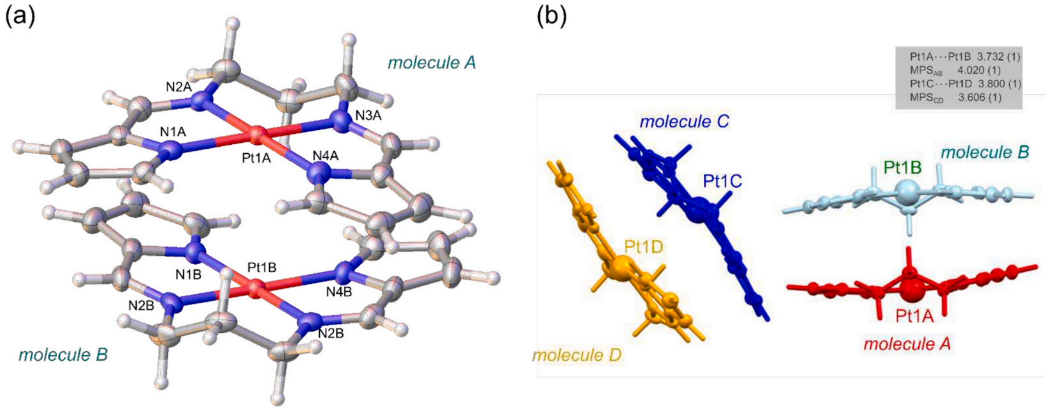

Fig. 1. (a) Partly labelled view of the X-ray structure of **1**. Two of the four independent molecules (A and B) in the asymmetric unit are illustrated. (b) View of the asymmetric unit of the crystal structure of **1** with the four independent molecules coloured according to their symmetry operators. The four molecules form two π···π dimers, with the molecules packed in a face-to-face manner with inverted relative orientation. Thermal ellipsoids are rendered at the 40% in (a) and 50% in (b), respectively. Hydrogen atoms are drawn as spheres with an arbitrary radius and Pt(II) ions are presented as spheres in b.

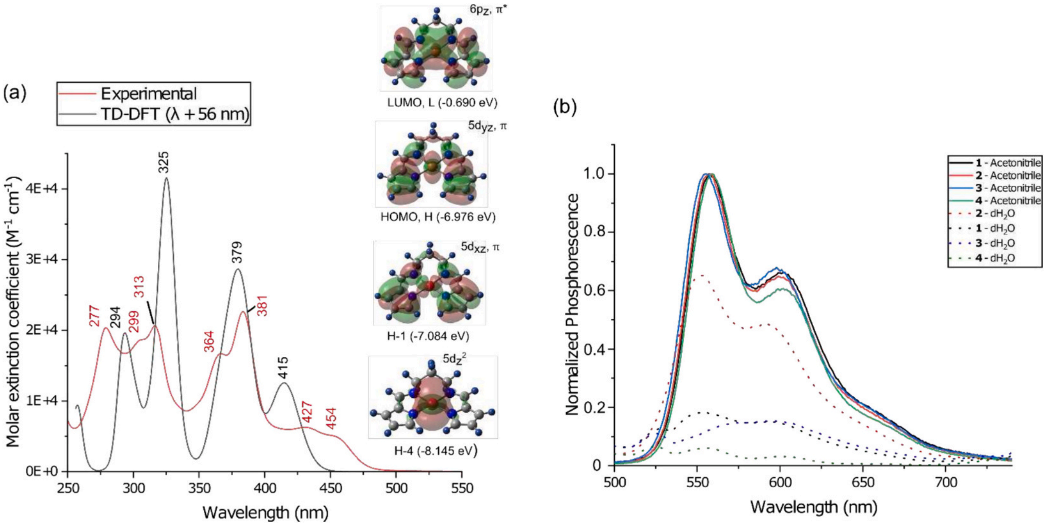

Fig. 2. (a) Experimental and DFT calculated (inset) electronic absorption spectra of **3** in acetonitrile. The absorption maxima (λ_{max}) are indicated for the experimental spectrum at 427, 380, 366, 313, 303 and 277 nm. The absorption envelope for the DFT calculated envelope spectrum of **3** is plotted from 200 to 450 nm and is plotted with a band width of 2000 cm^{-1} (full width at half maximum intensity, FWHM). The four key frontier MOs accounting for the bands at $\lambda > 325$ nm are shown. A full list of transition assignments is given in Tables S3–S5.† (b) Normalised emission spectra of **1–4** at 298 K in acetonitrile (**1**) black, (**2**) red, (**3**) blue and (**4**) green lines and in dH_2O (**1**) dashed black, (**2**) dashed red, (**3**) dashed blue, (**4**) dashed green lines. (For interpretation of the references to colour in this figure legend, the reader is referred to the web version of this article.)

(MOs) involved in the transition to the first excited state indicates it comprises 87% $_{1}$[Pt(5dyz),π → Pt(6pz),π*] character. The unoccupied MO is thus a metal–ligand wavefunction.

The visible region band at 381 nm is similar with 78% $_{1}$[Pt(5dxz),π → Pt(6pz),π*] character and a pronounced vibronic shoulder at 364 nm masking a weaker transition of mainly ligand π → π* character (HOMO−2 → LUMO, Table S3). The far-UV experimental bands are the most intense around 312 nm ($\varepsilon > 15{,}000$ M^{-1} cm^{-1}) and correlate with the 325 nm band of the TD-DFT spectrum. This transition is dominantly metal-to metal–ligand charge transfer (MMLCT) in character, i.e., 95% $_{1}$[Pt(5dz^{2}) → Pt(6pz),π*] with a satellite peak at 299 nm. Finally, the remaining band at 277 nm is assigned from the TD-DFT-calculated calculated spectrum at 298 nm, which comprises of two closely spaced transitions: 61% HOMO−2 → LUMO+1 and 50% HOMO−3 → LUMO. Significantly, the HOMO−3 → LUMO transition has part MLMLCT metal–ligand-to-metal–ligand charge transfer character because it originates from a MO which is a considerable admixture of the Pt 5dyz orbital with a *bis*(pyrrole-imine) π MO, i.e., $_{1}$[Pt(5dyz),π → Pt (6pz),π*].

The UV–vis spectra of complexes **1**–**4** were measured in acetonitrile and deionised water at 25 °C and are presented in Fig. S19. All four complexes exhibited intense absorption bands below 330 nm ($\varepsilon >$ 25,000 M^{-1} cm^{-1} in acetonitrile and > 20,000 M^{-1} cm^{-1} in dH_2O) and moderate to low intensity bands between 350 and 500 nm ($\varepsilon <$ 25,000 M^{-1} cm^{-1} in acetonitrile and < 20,000 M^{-1} cm^{-1} in dH_2O). The luminescence spectrum of Pt-chelates **1**–**4** (50 μM) in a fluid solution of acetonitrile and dH_2O are presented in Fig. 2b. Upon excitation, complexes **1**–**4** produced a yellow phosphorescent emission spectrum in both acetonitrile and aqueous solution. The luminescence spectra for the Pt(II) chelates in acetonitrile displayed a structured profile with a peak maximum at ∼560 nm and a shoulder at ∼610 nm (Fig. 2b).

Our emission spectra are in agreement with studies of previously reported Pt(II)-*bis* (pyrrole-imine) chelates [4,49,71]. The solubility of complexes **1**, **3**, and **4** was significantly lower compared to that of complex **2**. This difference was spectroscopically apparent in the luminescent emission spectra of complexes **1**, **3**, and **4** (Fig. 2b), where poor resolution of the peaks and band broadening were observed. In contrast, complex **2** possessed a well-defined luminescence emission spectrum. A likely explanation for this characteristic is that complex **2** contains an OH motif, contributing to an increased solubility of the complex in an aqueous medium [72].

5.3. *Apparent quantum yields of the Pt(II) Schiff base chelates*

To provide further support for the luminescent characteristics exhibited by complexes **1**–**4**, we conducted luminescent emission spectrum measurements in both acetonitrile and dH_2O in the absence of $^3O_2$ (Fig. S15). The elimination of $^3O_2$ yielded a noteworthy enhancement in the luminescent emission of complexes **1**–**4** (Table S7). The increase in emission can be attributed to the removal of $^3O_2$, indicating that the luminescence of complexes **1**–**4** hinges on phosphorescence from a triplet excited state. For phosphorescent molecules $^3O_2$ quenches the phosphorescence by a direct energy transfer mechanism, where energy from **1 to 4** converts $^3O_2$ to $^1O_2$ [27,36]. Consequently, the removal of $^3O_2$ led to a heightened luminescent emission.

To provide a more precise description of the luminescent properties of compounds **1**–**3**, we conducted a comparative analysis of their quantum yields by a relative method (ΦF) in various environments, including DCM, their interaction with HSA, and both aerobic and anaerobic conditions in acetonitrile and dH_2O. A summary of the ΦF data is presented in Tables S6 and S7. Complexes **1** and **2** had the highest ΦF in dH_2O 0.040(± 0.0021) and 0.065(± 0.0042), respectively. While **3** and **4** had the highest ΦF in DCM 0.022(±0.0006) and 0.024 (±0.0013) respectively. Overall, complexes **1**–**3** had low ΦF emissions in aerobic solvents (ΦF ranging from 0.0052 to 0.065) and **1**–**2** had moderate ΦF in anaerobic dH_2O (ΦF ranging from 0.20 to 0.43). When compounds **1**–**3** were bound to HSA, a significant enhancement in ΦF was observed. This enhancement can be attributed to the removal of molecular oxygen ($^3O_2$), which has a quenching effect on phosphorescence. Consequently, the structural and spectral properties of **1**–**3** were compared to those of **4**, revealing microsecond lifetimes [4]. The luminescence emission of **1**–**3** is assigned to phosphorescence from [3] LC excited state and [1,3]MLCT states as was reported for complex **4** by Shan et al. [4]

5.4. *Pt(II) chelates binding to HSA*

The Pt(II) chelates investigated in this study have previously demonstrated a moderate binding affinity to HSA ranging from 10^3 to 10^5 M^{-1} [48,49]. It is well-documented that certain luminescent metal complexes exhibit enhanced luminescence upon binding to HSA [23,73]. To assess the luminescent properties of the Pt(II) chelates in this study, we incubated 5 μM of each complex with 5 μM of HSA. Notably, molecules **1**, **2**, and **3** displayed a significant increase in phosphorescence intensity upon binding to HSA, as depicted in Figs. 3a and S15. The quantum yield of HSA···**1**, HSA···**2** and HSA···**3** adducts increased by 15.6, 4.26 and 12.2-fold, respectively (Table S6) in comparison to the free molecules. This was coupled with a red shift in the emission spectra of ∼3 nm. Complex **4** had very weak phosphorescence intensities aqueous solution, even when bound to HSA.

Among the four complexes studied, complex **1** exhibited the most significant enhancement in quantum yield when bound to HSA, as illustrated in Fig. 3a and detailed in Table S6. The unbound complex had a ΦF of 0.0052 in acetonitrile. However, when bound to HSA, the ΦF increased significantly to 0.62, representing a remarkable 119-fold enhancement. Given the heightened sensitivity of **1** to luminescent enhancement in the presence of HSA, we proceeded to assess its limit of detection (LOD) for HSA detection (Fig. 3b).

The results indicated that HSA could be detected at concentrations as low as 5 nM, with a linear detection range of 5–29 nM in a KH_2PO_4 buffer. Notably, this LOD for HSA detection aligns with other probes designed for HSA detection, such as thieno[3,2-*b*]pyridine-5(4H)-one [74].

5.5. *Cytotoxicity evaluation of the target compounds*

The synthesised Pt(II) chelates **1**–**3** were assessed for their antiproliferative activities on the hormone responsive (MCF-7) and non-transformed NMuMG cells using 3-(4,5-dimethylthiazol-2-yl) − 2,5-diphenyltetrazolium bromide (MTT) assay keeping plumbagin as positive control (Fig. S20) [63]. The growth inhibition graphs for the tested cells, at varying concentrations (5 to 250 μM) of the synthesised compounds, are displayed in Figs. 4 and S21. It is evident that the activity depends on the nature of the moiety on the linking carbon chain. Complex **1** (Fig. 4a) shows a significant dose-dependent reduction of cell viability of MCF-7 cells, while only reducing the viability of NMuMG cells below 50% at higher concentrations (> 100 μM). The cytotoxicity of difference of **1** for MCF-7 breast cancer cells compared to non-transformed NMuMG cells suggests a possible specificity to highly proliferative cancer cells and potential as a therapeutic compound. Complex **2** (Fig. S21) showed little cytotoxicity, not reaching 50% growth inhibition at any concentrations tested, while complex **3** was only cytotoxic at 250 μM. The inactivity of complex **2** may be attributed to the OH functional group on the second position of the propyl *bis*(imine) linkage. The OH group is an electron withdrawing group and could be favourable for uptake by cellular mechanisms such as the efflux pump which is known to detoxify cells of toxic compounds [75].

All three Pt(II) complexes were assessed as PDT agents (Figs. 4 and S21). Only complex **3** indicated potential to be used as a photosensitiser (PS, i.e., a class of PDT's; Fig. 4c). Complex **3** showed little reduction in cell viability at lower concentrations in both cell lines, but after UV light exposure (λ^{ex}, 355 nm) there is a significant dose-dependent reduction in the viability of MCF-7 cells, but not NMuMG cells. This suggests possible specificity to highly proliferative cancer cells after UV exposure, which justifies further investigation of complex **3** as a PS therapeutic compound. Complex **1** indicated no significant enhancement in cytotoxicity when irradiated with UV-light. In summary, only **1** and **3** (when irradiated with UV light) exhibited sufficient cytotoxicity to accurately delineate their IC_{50} concentrations, which were∼ 25 uM, respectively. This conclusion assumes that all three Pt(II) chelates produce the same amount of ROS, when irradiated with UV light (λ^{ex}, 355 nm).

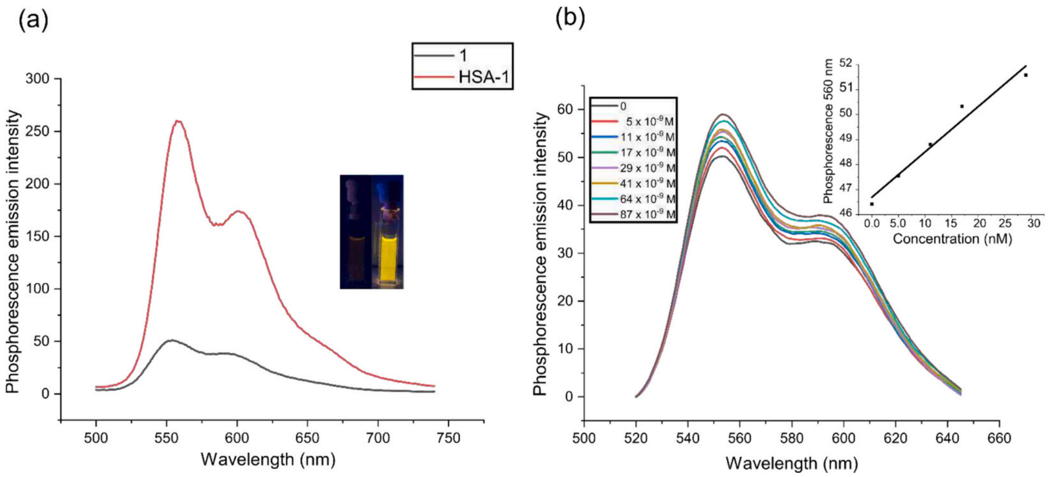

Fig. 3. (a) Fluorescence spectrum of **1** in the presence and absence of HSA in KH_2PO_4 buffer (50 mM, pH 7.5). (b) Fluorescence spectrum of **1** upon increasing concentrations of HSA (0–87 μM) in KH_2PO_4 buffer (50 mM, pH 7.5). The insert is the linear relationship of the change in phosphorescence emission intensity of **1** at 560 nm vs HSA concentration (0–29 μM).

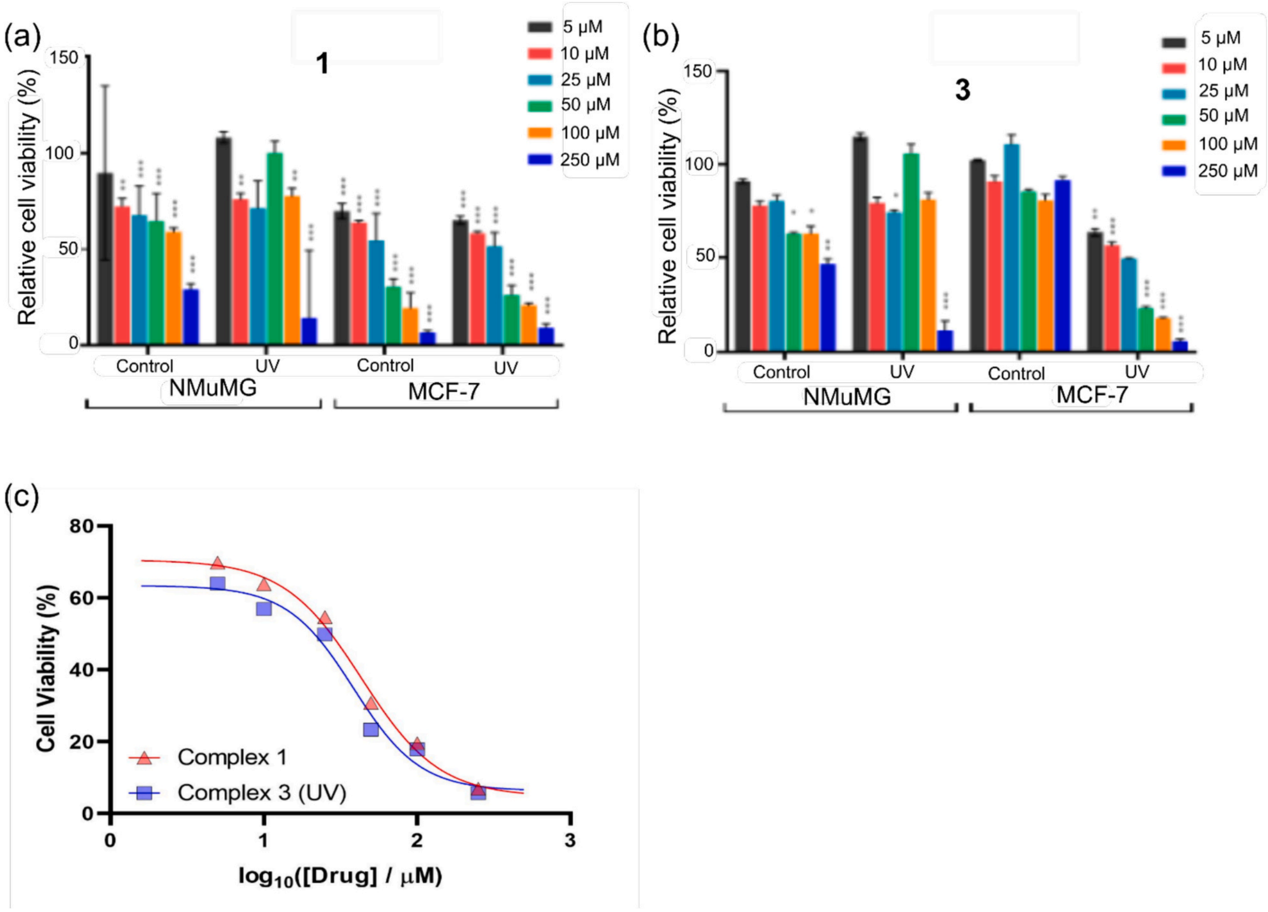

Fig. 4. Relative cell viability graphs represent the changes in cell viability percentage of NMuMG and MCF-7 cells in response to treatment with increasing concentrations of Pt(II) complexes **1** (a), **3** (b) relative to a vehicle control. Changes in viability were measured with and without exposure to UV light. Error bars represent standard deviation ($n = 3$). Statistical significance was assessed using the Student's *t*-test, where * $p < 0.05$, ** $p < 0.01$, and *** $p < 0.001$. (c) Cell viability percentage MCF-7 cells in response to treatment with increasing concentrations of complexes **1** (absence of UV exposure and **3** (UV-exposed) fitted with a Hill fit plot in order to delineate the IC_{50} concentrations.

5.6. *Intracellular fluorescence of Pt(II) chelates*

As the Pt(II) complexes emitted radiation with an enhanced quantum yield when bound to HSA, we evaluated them as photosensitisers. The intracellular fluorescence of Pt(II) complexes **1**–**3** was measured using fluorescence microscopy, shown in Fig. S22. **1** and **3** show high levels of cytoplasmic fluorescence, demonstrating cellular uptake in the absence of HSA. With the addition of HSA, intracellular fluorescence was reduced. A potential explanation is that HSA had transported the Pt(II) chelates **1** and **3** towards a certain target, and therefore quenching **1** and **3** phosphorescence. Unsurprisingly complex **2** showed a lower cellular uptake and a slight reduction with the addition of HSA. The lack of nuclear localisation suggests that changes in cell viability are not likely due to direct interaction with DNA, although interaction with cytoplasmic components is possible. Further interpretation of cellular localization is limited by the resolution of the imaging technique used.

5.7. Molecular docking studies

Molecular docking was employed as a potential method to elucidate why only complex **3** behaved as a PS agent. The binding affinity descriptor (ΔG_{bind}) of the complexes to bovine serum albumin (BSA) is reported in Table S8, demonstrating favourable comparison with our experimental data for the same Pt(II) complexes binding to HSA [48,49]. For the molecular docking studies, BSA was considered, as it is present in the foetal bovine serum (FBS) used to grow both the MCF-7 and NMuMG cell lines. BSA shares 80% homology with HSA and comprises three domains (I, II, and III), divided into two subdomains (A and B) [76]. Therefore, it is likely that the Pt(II) chelates bind to both HSA and BSA through a similar mechanism and to similar binding sites. Molecular docking analysis reveals that complex **3** binds to subdomain IB, a cleft region located near the surface of BSA (Fig. 5). Notably, this subdomain is not one of the protein's major drug binding sites.

This observation provides insight into why the ΔG_{bind} scores and experimental binding data indicate lower binding affinity for complex **3** to HSA compared to both complexes **1** and **2**, respectively. The molecular docking results for complexes **1** and **2** suggest a preference for binding to subdomain IIIA, which is one of BSA's major drug binding sites. This drug-binding site is situated within the hydrophobic core of BSA, as illustrated in Fig. S23.

Based on the predicted binding sites elucidated from the molecular docking results (Fig. 5), we speculate that all three Pt(II) chelates analysed for their cytotoxic potential bind to BSA. Since complex **3** binds close to the protein's surface, it readily absorbs the UV light (λ^{ex}, 355 nm) with which it is irradiated. Upon irradiation of complex **3**, it transitions from a singlet state to a long-lived triplet state. The triplet state, more stable than the excited singlet state, has a longer lifetime [78,79].

This extended lifetime is essential for PDT as it allows the triplet state of complex **3** to transfer its energy to molecular oxygen [79]. This transfer of energy can occur through two reactions, Type 1 and Type 2. In a Type 1 reaction, the electron transfers from the triplet state PS to either H_2O_2 or O_2, resulting in the formation of a hydroxy radical (OH•) or a superoxide anion (O_2•−). A Type II reaction involves the conversion of $^3O_2$ to $^1O_2$ [78–80]. While both reaction mechanisms are plausible for PDTs, Type II reactions are more common. The resulting reactive oxygen species (ROS) damage cell membranes and induce apoptosis in cancer cells [78]. Complexes **1** and **2** bind to BSA in subdomain IIIA, which is a hydrophobic cavity embedded in the protein. This means limited diffusion of triplet oxygen to the buried Pt(II) chelates and can account for their lower cytotoxicity since singlet oxygen generation will decrease for such buried photosensitizers. The opposite will hold true for surface-bound metal chelate photosensitizers. Furthermore, if ROS species are generated, they are more likely to interact with surrounding amino acid residues, leading to protein carbonylation [81].

An alternative explanation as to why complex **3** behaves as a PS as opposed to complexes **1** and **2**, is that it is more hydrophobic. This characteristic aligns with the typical requirement for PDT agents, as hydrophobic molecules can efficiently diffuse into tumour cells and localise within intracellular membranes. Previous studies have reported that some highly effective PS agents bind to low-density lipoprotein (LDL). Given the overexpression of LDL receptors on tumour cells, PS agents utilise LDL as a transport protein to reach the target site, where they can be "activated" by UV light [82,83]. This proposed mechanism could be applicable to complex **3** if it readily binds to LDL and is transported to the tumour cell. Upon UV light irradiation, the resulting ROS would lie within the optimal threshold distance of 10–55 nm from the cell membrane to be most effective. In this scenario, the ROS would damage the cell membrane, ultimately leading to apoptosis [84].

6. Conclusions

Four Pt(II) chelates were successfully synthesised (**1**–**4**), of which we obtained the novel crystal structure of complex **1**. The electronic spectra of the complex were assigned using TD-DFT simulations. Thereafter, we assessed the photophysical properties of the Pt(II) chelates by measuring their apparent quantum yield in various solvents and when bound to HSA. Complex **1** had a 119-fold quantum yield enhancement when bound to HSA and was able to detect HSA concentrations as low as 5 nM. Finally, we assessed the potential cytotoxicity of Pt(II) complexes **1**–**3** as therapeutics and as PS. The MTT assay results indicated that complex **1** was cytotoxic, regardless of UV light exposure. Surprisingly, complex **3** behaved as a PS and was cytotoxic only when irradiated with UV light.

CRediT authorship contribution statement

Sheldon Sookai: Writing – review & editing, Writing – original draft, Project administration, Methodology, Investigation, Formal analysis, Data curation, Conceptualization. **Shanen Perumal:** Writing – original draft, Methodology, Investigation, Formal analysis. **Mandeep Kaur:** Writing – review & editing, Supervision, Funding acquisition, Formal analysis. **Orde Q. Munro:** Writing – review & editing, Supervision, Resources, Project administration, Funding acquisition,

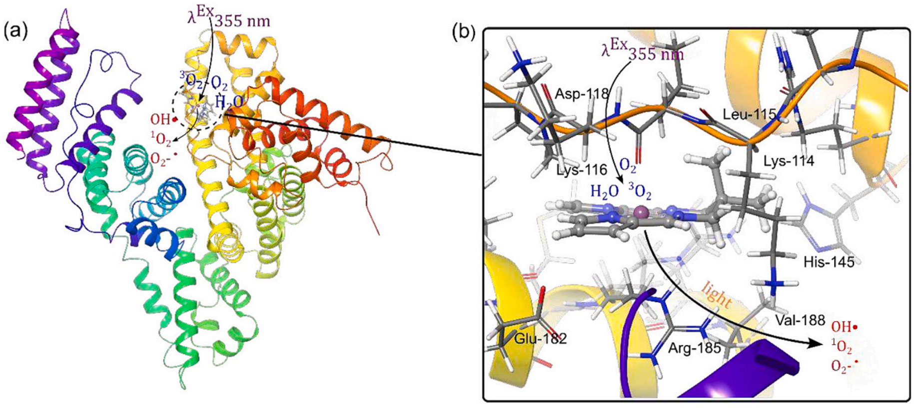

Fig. 5. Complex **3** docked into the cleft of subdomain IB of BSA (PDB 4F5S) [77]. Site IB lies close to the surface of the protein. Any complex bound to this site is likely to absorb UV light and produce ROS.

Conceptualization.

Declaration of competing interest

The authors declare the following financial interests/personal relationships which may be considered as potential competing interests:

Sheldon Sookai reports financial support was provided by National Research Foundation. Orde Q Munro reports financial support was provided by National Research Foundation. Mandeep Kaur reports financial support was provided by National Research Foundation. Shanen Perumal reports financial support was provided by National Research Foundation. If there are other authors, they declare that they have no known competing financial interests or personal relationships that could have appeared to influence the work reported in this paper.

Data availability

Data will be made available on request.

Acknowledgements

This work is based on research supported by the South African Research Chairs Initiative of the Department of Science and Innovation (DSI) and National Research Foundation (NRF) of South Africa (Grant No 64799, OQM). The authors thank WITS University and the NRF for funding to purchase a JASCO J-1500 MCD spectrometer (Grant No 116177, OQM) and a dual-wavelength Bruker D8 Venture X-ray diffractometer (Grant No 129920, OQM). We also thank the Centre for High Performance Computing (Project CHEM1065, CHPC, Cape Town) for both the CPU time and resources needed for the DFT simulations. The authors would like to acknowledge Manuel Fernandes for aiding in the deposition of the crystal structure to the CSD and Helder Marques for his invaluable input into the manuscript.

Appendix A. Supplementary data

Electronic Supplementary Information (ESI) available: Complete experimental details and supplementary tables and figures in PDF format, X-ray crystal structures in CIF format (CCDC 2310554). Supplementary data to this article can be found online at [https://doi.org/10.1016/j.jinorgbio.2024.112617].

References

[1] R.U. Braun, K. Zeitler, T.J.J. Müller, Org. Lett. 3 (2001) 3297–3300.
[2] C.E. Hewton, M.C. Kimber, D.K. Taylor, Tetrahedron Lett. 43 (2002) 3199–3201.
[3] K. Li, G.S.M. Tong, Q. Wan, G. Cheng, W.-Y. Tong, W.-H. Ang, W.-L. Kwong, C.-M. Che, Chem. Sci. 7 (2016) 1653–1673.
[4] X.-F. Shan, D.-H. Wang, C.-H. Tung, L.-Z. Wu, Tetrahedron 64 (2008) 5577–5582.
[5] S.S. Razi, Y.H. Koo, W. Kim, W. Yang, Z. Wang, H. Gobeze, F. D'Souza, J. Zhao, D. Kim, Inorg. Chem. 57 (2018) 4877–4890.
[6] W. Zhang, N.H. Lee, E.N. Jacobsen, J. Am. Chem. Soc. 116 (1994) 425–426.
[7] S. Banerjee, M.S. Capper, G.J. Clarkson, H. Huang, P.J. Sadler, Polyhedron 172 (2019) 157–166.
[8] J. Deng, J. Wang, M. Khan, P. Yu, F. Yang, H. Liang, J. Inorg. Biochem. 185 (2018) 10–16.
[9] Q.-P. Qin, Z.-F. Wang, X.-L. Huang, M.-X. Tan, B.-Q. Zou, H. Liang, Eur. J. Med. Chem. 184 (2019) 111751.
[10] A. Hamil, K. Khalifa, A. Almutaleb, M. Nouradean, Adv. J. Chem.-Sect. A 3 (2020) 524–533.
[11] D. Bandyopadhyay, M. Layek, M. Fleck, R. Saha, C. Rizzoli, Inorg. Chim. Acta 461 (2017) 174–182.
[12] G.A. Krishna, T.M. Dhanya, A.A. Shanty, K.G. Raghu, P.V. Mohanan, J. Mol. Struct. 1274 (2023) 134384.
[13] A. Jarrahpour, D. Khalili, E. De Clercq, C. Salmi, J.M. Brunel, Molecules 12 (2007) 1720–1730.
[14] E. Wong, C.M. Giandomenico, Chem. Rev. 99 (1999) 2451–2466.
[15] X. Yao, K. Panichpisal, N. Kurtzman, K. Nugent, Am J Med Sci 334 (2007) 115–124.
[16] M.P. Barr, S.G. Gray, A.C. Hoffmann, R.A. Hilger, J. Thomale, J.D. O'Flaherty, D. A. Fennell, D. Richard, J.J. O'Leary, K.J. O'Byrne, PLoS One 8 (2013) e54193.
[17] A.K. Godwin, A. Meister, P.J. O'Dwyer, C.S. Huang, T.C. Hamilton, M.E. Anderson, Proc. Natl. Acad. Sci. 89 (1992) 3070–3074.
[18] T.C. Johnstone, K. Suntharalingam, S.J. Lippard, Chem. Rev. 116 (2016) 3436–3486.
[19] Y. Shi, S.-A. Liu, D.J. Kerwood, J. Goodisman, J.C. Dabrowiak, J. Inorg. Biochem. 107 (2012) 6–14.
[20] Y.-R. Zheng, K. Suntharalingam, T.C. Johnstone, S.J. Lippard, Chem. Sci. 6 (2015) 1189–1193.
[21] F.-U. Rahman, A. Ali, H.-Q. Duong, I.U. Khan, M.Z. Bhatti, Z.-T. Li, H. Wang, D.-W. Zhang, Eur. J. Med. Chem. 164 (2019) 546–561.
[22] T. Chatzisideri, S. Thysiadis, S. Katsamakas, P. Dalezis, I. Sigala, T. Lazarides, E. Nikolakaki, D. Trafalis, O.A. Gederaas, M. Lindgren, V. Sarli, Eur. J. Med. Chem. 141 (2017) 221–231.
[23] P. Zhang, H. Huang, S. Banerjee, G.J. Clarkson, C. Ge, C. Imberti, P.J. Sadler, Angew. Chem. Int. Ed. 58 (2019) 2350–2354.
[24] R. Guan, Y. Chen, L. Zeng, T.W. Rees, C. Jin, J. Huang, Z.-S. Chen, L. Ji, H. Chao, Chem. Sci. 9 (2018) 5183–5190.
[25] M.-H. Chen, Y. Zheng, X.-J. Cai, H. Zhang, F.-X. Wang, C.-P. Tan, W.-H. Chen, L.-N. Ji, Z.-W. Mao, Chem. Sci. 10 (2019) 3315–3323.
[26] W. Lv, Z. Zhang, K.Y. Zhang, H. Yang, S. Liu, A. Xu, S. Guo, Q. Zhao, W. Huang, Angew. Chem. Int. Ed. 55 (2016) 9947–9951.
[27] S. Monro, K.L. Colón, H. Yin, J. Roque, P. Konda, S. Gujar, R.P. Thummel, L. Lilge, C.G. Cameron, S.A. McFarland, Chem. Rev. 119 (2019) 797–828.
[28] Z. Zhao, P. Gao, Y. You, T. Chen, Chem. Eur. J. 24 (2018) 3289–3298.
[29] H.K. Saeed, P.J. Jarman, S. Archer, S. Sreedharan, I.Q. Saeed, L.K. Mckenzie, J. A. Weinstein, N.J. Buurma, C.G.W. Smythe, J.A. Thomas, Angew. Chem. 129 (2017) 12802–12807.
[30] S. Imstepf, V. Pierroz, R. Rubbiani, M. Felber, T. Fox, G. Gasser, R. Alberto, Angew. Chem. 128 (2016) 2842–2845.
[31] A.P. King, S.C. Marker, R.V. Swanda, J.J. Woods, S.-B. Qian, J.J. Wilson, Chem. Eur. J. 25 (2019) 9206–9210.
[32] Z.-Y. Pan, C.-P. Tan, L.-S. Rao, H. Zhang, Y. Zheng, L. Hao, L.-N. Ji, Z.-W. Mao, Angew. Chem. 132 (2020) 18914–18921.
[33] S. Lazic, P. Kaspler, G. Shi, S. Monro, T. Sainuddin, S. Forward, K. Kasimova, R. Hennigar, A. Mandel, S. McFarland, L. Lilge, Photochem. Photobiol. 93 (2017) 1248–1258.
[34] P. Zhang, H. Huang, Dalton Trans. 47 (2018) 14841–14854.
[35] E.C. Glazer, Photochem. Photobiol. 93 (2017) 1326–1328.
[36] I. Ashur, R. Goldschmidt, I. Pinkas, Y. Salomon, G. Szewczyk, T. Sarna, A. Scherz, J. Phys. Chem. A 113 (2009) 8027–8037.
[37] C.-P. Tan, Y.-M. Zhong, L.-N. Ji, Z.-W. Mao, Chem. Sci. 12 (2021) 2357–2367.
[38] J. Tang, H.-Y. Yin, J.-L. Zhang, in: K.K.-W. Lo (Ed.), Inorganic and Organometallic Transition Metal Complexes with Biological Molecules and Living Cells, Academic Press, 2017, pp. 1–53.
[39] A. de Almeida, R. Bonsignore, Bioorg. Med. Chem. Lett. 30 (2020) 127219.
[40] Y. Dai, Z. Yang, S. Cheng, Z. Wang, R. Zhang, G. Zhu, Z. Wang, B.C. Yung, R. Tian, O. Jacobson, C. Xu, Q. Ni, J. Song, X. Sun, G. Niu, X. Chen, Adv. Mater. 30 (2018) 1704877–1704885.
[41] S.S. Taneja, J. Bennett, J. Coleman, R. Grubb, G. Andriole, R.E. Reiter, L. Marks, A.-R. Azzouzi, M. Emberton, J. Urol. 196 (2016) 1096–1104.
[42] G.S. Kulkarni, L. Lilge, M. Nesbitt, R.J. Dumoulin-White, A. Mandel, M.A.S. Jewett, Eur. Urol. Open Sci. 41 (2022) 105–111.
[43] S. Curry, Drug Metab. Pharmacokinet. 24 (2009) 342–357.
[44] G.J. Quinlan, G.S. Martin, T.W. Evans, Hepatology 41 (2005) 1211–1219.
[45] O.V. Dolomanov, L.J. Bourhis, R.J. Gildea, J.A.K. Howard, H. Puschmann, J. Appl. Crystallogr. 42 (2009) 339–341.
[46] G.M. Sheldrick, Acta Crystallogr. Sect. Found. Adv. 71 (2015) 3–8.
[47] G.M. Sheldrick, Acta Crystallogr. Sect. C Struct. Chem. 71 (2015) 3–8.
[48] S. Sookai, O.Q. Munro, ChemistryEurope 1 (2023) e202300012.
[49] S. Sookai, O.Q. Munro, Dalton Trans. 52 (2023) 14774–14789.
[50] C. Würth, M. Grabolle, J. Pauli, M. Spieles, U. Resch-Genger, Nat. Protoc. 8 (2013) 1535–1550.
[51] S. Fery-Forgues, D. Lavabre, J. Chem. Educ. 76 (1999) 1260.
[52] J. A. Riddick, W. B. Bunger and T. K. Sakano.
[53] M.J. Frisch, G.W. Trucks, H.B. Schlegel, G.E. Scuseria, M.A. Robb, J.R. Cheeseman, G. Scalmani, V. Barone, G.A. Petersson, H. Nakatsuji, X. Li, M. Caricato, A. V. Marenich, J. Bloino, B.G. Janesko, R. Gomperts, B. Mennucci, H.P. Hratchian, J. V. Ortiz, A.F. Izmaylov, J.L. Sonnenberg, D. Williams-Young, F. Ding, F. Lipparini, F. Egidi, J. Goings, B. Peng, A. Petrone, T. Henderson, D. Ranasinghe, V. G. Zakrzewski, J. Gao, N. Rega, G. Zheng, W. Liang, M. Hada, M. Ehara, K. Toyota, R. Fukuda, J. Hasegawa, M. Ishida, T. Nakajima, Y. Honda, O. Kitao, H. Nakai, T. Vreven, K. Throssell, J.A. Montgomery Jr., J.E. Peralta, F. Ogliaro, M. J. Bearpark, J.J. Heyd, E.N. Brothers, K.N. Kudin, V.N. Staroverov, T.A. Keith, R. Kobayashi, J. Normand, K. Raghavachari, A.P. Rendell, J.C. Burant, S.S. Iyengar, J. Tomasi, M. Cossi, J.M. Millam, M. Klene, C. Adamo, R. Cammi, J.W. Ochterski, R.L. Martin, K. Morokuma, O. Farkas, J.B. Foresman, D.J. Fox, Gaussian 16 Revision C.01, 2016.
[54] T. Yanai, D.P. Tew, N.C. Handy, Chem. Phys. Lett. 393 (2004) 51–57.
[55] F. Weigend, R. Ahlrichs, Phys. Chem. Chem. Phys. 7 (2005) 3297–3305.
[56] S. Grimme, S. Ehrlich, L. Goerigk, J. Comput. Chem. 32 (2011) 1456–1465.
[57] P. Fuentealba, H. Preuss, H. Stoll, L. Von Szentpály, Chem. Phys. Lett. 89 (1982) 418–422.
[58] J.R. Cheeseman, G.W. Trucks, T.A. Keith, M.J. Frisch, J. Chem. Phys. 104 (1996) 5497–5509.
[59] R. Ditchfield, Mol. Phys. 27 (1974) 789–807.

[60] F. Lipparini, G. Scalmani, B. Mennucci, E. Cancès, M. Caricato, M.J. Frisch, J. Chem. Phys. 133 (2010) 014106.

[61] R. Dennington, T.A. Keith, J.M. Millam, GaussView Version 6, 2019.

[62] N.M. O'boyle, A.L. Tenderholt, K.M. Langner, J. Comput. Chem. 29 (2008) 839–845.

[63] S. Sagar, L. Esau, B. Moosa, N.M. Khashab, V.B. Bajic, M. Kaur, Anti-Cancer Agents Med. Chem. Former. Curr. Med. Chem.-Anti-Cancer Agents 14 (2014) 170–180.

[64] S. Sookai, M.L. Bracken, M. Nowakowska, Molecules 28 (2023) 7466–7495.

[65] J.R.L. Priqueler, I.S. Butler, F.D. Rochon, Appl. Spectrosc. Rev. 41 (2006) 185–226.

[66] A. Albinati, F. Lianza, P.S. Pregosin, B. Mueller, Inorg. Chem. 33 (1994) 2522–2526.

[67] B.M. Still, P.G. Anil Kumar, J.R. Aldrich-Wright, W.S. Price, Chem. Soc. Rev. 36 (2007) 665–686.

[68] M. Karplus, J. Chem. Phys. 30 (2004) 11–15.

[69] I.M. Ismail, S.J.S. Kerrison, P.J. Sadler, Polyhedron 1 (1982) 57–59.

[70] A. Bondi, J. Phys. Chem. 68 (1964) 441–451.

[71] H.-F. Xiang, S.-C. Chan, K.K.-Y. Wu, C.-M. Che, P.T. Lai, Chem. Commun. (2005) 1408–1410.

[72] C. Ni, X. Ma, Z. Pang, P. Guo, Z. Yang, J. Chem. Eng. Data 68 (2023) 3411–3422.

[73] R. Wang, X. Li, J. Yoon, ACS Appl. Mater. Interfaces 13 (2021) 19543–19571.

[74] S. Lee, D.-B. Sung, S. Kang, S. Parameswaran, J.-H. Choi, J.S. Lee, M.S. Han, Sensors 19 (2019) 5298–5311.

[75] I.G. Darvey, Biochem. Educ. 27 (1999) 209–210.

[76] S. Ketrat, D. Japrung, P. Pongprayoon, J. Mol. Graph. Model. 98 (2020) 107601–107609.

[77] A. Bujacz, Acta Crystallogr. D Biol. Crystallogr. 68 (2012) 1278–1289.

[78] H. Abrahamse, M.R. Hamblin, Biochem. J. 473 (2016) 347–364.

[79] C.S. Foote, Science 162 (1968) 963–970.

[80] M. Hayyan, M.A. Hashim, I.M. AlNashef, Chem. Rev. 116 (2016) 3029–3085.

[81] C.A. Juan, J.M. Pérez de la Lastra, F.J. Plou, E. Pérez-Lebeña, Int. J. Mol. Sci. 22 (2021) 4642–4663.

[82] A.K. Iyer, K. Greish, T. Seki, S. Okazaki, J. Fang, K. Takeshita, H. Maeda, J. Drug Target. 15 (2007) 496–506.

[83] D. Kessel, J. Photochem. Photobiol. B 14 (1992) 261–262.

[84] J.S. Dysart, M.S. Patterson, Phys. Med. Biol. 50 (2005) 2597–2618.